http://ansinet.com/itj

ITJ

ISSN 1812-5638

INFORMATION TECHNOLOGY JOURNAL

ANSInet
Asian Network for Scientific Information
308 Lasani Town, Sargodha Road, Faisalabad - Pakistan

Information Technology Journal 11 (2): 181-190, 2012
ISSN 1812-5638 / DOI: 10.3923/itj.2012.181.190
© 2012 Asian Network for Scientific Information

Effects of Upper Rivulet During Rain-wind Induced Vibration

P. Xie, C.Y. Zhou, J.Y. Zhu and C. Wang
Harbin Institute of Technology, Shenzhen Graduate School,
Shenzhen University Town, Shenzhen 518055, China

Abstract: Rain-wind-induced Vibration (RWIV) appearing on cable stayed bridges involves complicated fluid and structure interactions and its mechanism is not fully understood. It is believed that the upper-rivulet which is often seen when the RWIV occurs plays an important role. In this study, the effects of the upper rivulet to the aerodynamic forces on the cable and flow pattern around it were numerically investigated. Different azimuths of the attached upper rivulet ranged from 0 to 60° were involved. The result showed that as the rivulet located at different position the boundary layer changed a lot and the forces on the cable and the flow patterns of the wake behind the cable were so that changed.

Key words: Rain-wind induced vibration, large eddy simulation, flow pattern, strouhal number, cable stayed bridge, rivulet attached cable

INTRODUCTION

Rain-wind Induced Vibration (RWIV) is a kind of instability that appears on cable stayed bridges under rainy weather even with a low wind speed. Hikami and Shiraishi (1988) first reported this phenomenon. They observed the upper and lower water rivulets on the surface of the stayed cable when RWIV happened. Matsumoto *et al*. (1995, 2003) classified RWIV into three types, the "galloping" type, the vortex shedding type and their mixed type. They believed that the most important incentives for RWIV were firstly the "upper water rivulet" and/or "axial flow" and secondly the three-dimensionality of conventional Karman vortex shedding along the cable axis. Having realized the importance of the rivulets, many researchers tried to interpret such an inducement. Rivulets effect was experimentally studied by Bosdogianni and Olivari (1996) where, two attached bars on cylinder surface were used to represent the rivulets and a strong increase in the amplitude of the cylinder oscillation was observed. Zhan *et al*. (2008) carried out an experiment for a cable with artificial rivulets in wind tunnel, in which the effects of the inclination as well as the yaw angle of the cable orientation were considered. They found that the vortex-shedding-induced vibration occurred at a very low wind speed and the Strouhal number of an inclined cable was different from that of a horizontal one. They also observed that the galloping occurred when the artificial rivulet was placed at certain positions. More experiments were carried out by Alam and Zhou (2006, 2007) to study the fluid dynamics around an inclined circular cylinder with and without water running over its surface. It was found that the rivulet running over the cylinder surface behaved quite differently depending on the reynolds number which subsequently impacted greatly upon the fluid dynamics around the cylinder. Further experimental investigation (Alam *et al*., 2010) was conducted about the wake of a circular cylinder with two tripwires. By analyzing the aerodynamic forces on the cylinder for different tripwire azimuth angles, it was pointed out that a bi-stable phenomenon may be closely linked with rain-wind-induced cable vibration.

Though it is now known that the RWIV is caused by the combined interactions between rain, wind and cable-rivulet structure itself and the upper rivulet plays an important role in the interaction. However, the mechanism of this complicated fluid-structure interaction is not fully understood yet. Numerical simulation of flow around rivulet attached cable will help gaining more knowledge about this. Flow field around different kinds of bluff body and body combinations were numerically studied in the past, briefly as in So *et al*. (2001), Shirani (2001), Benazza *et al*. (2007) and Islam and Zhou (2009) and the issue that involved cross flow past circular cylinder was mainly concerned, in most of which the aerodynamic forces and flow patterns were analyzed. However, the structure of a cylinder with an attachment on its surface which a RWIV can be modeled into, was seldom reported. One of the few was done by Li *et al*. (2010) who treated the oscillation of the cable as a given moving boundary. By applying the moving boundary condition into a 2-D simulation model, the transient aerodynamic

Corresponding Author: C.Y. Zhou, Harbin Institute of Technology, Shenzhen Graduate School, Shenzhen University Town, Shenzhen 518055, China

forces of the cable with a predetermined cable oscillation was obtained. Another 2-D model was developed by Robertson *et al*. (2010) to evaluate the formation of a thin film of water on the surface of a horizontal circular cylinder. As it is seen, those simulated results about RWIV were restricted to 2-D. To the best of our knowledge, 3-D simulation of flow around rivulet attached cable was not seen. Accordingly, a numerical investigation about the 3-D flow around a RWIV model was carried out in this study. In the RWIV model, the cable was represented by a circular cylinder and the upper rivulet was replaced by an attached arch. The 3-D transient flow fields around the models with different rivulet attached angles were simulated using Large-eddy Simulation (LES) method. By representing the flow field around the cable when RWIV happened and analyzing the forces characteristics of the cable, it was hoped to uncover the affection of upper rivulet during a RWIV.

NUMERICAL METHOD

Physical model: To simulate a cable with upper rivulet, a cylinder with an elliptical arch attachment is considered as shown in Fig. 1, where, D is the diameter of the cylinder, U is the velocity of the uniform incident flow, L, h and θ are the width, height and azimuth of rivulet attachment, respectively and S_0 represents the front stagnation point. The values of L and h are set as $\pi D/24$ and D/20, respectively which are comparable to those values reported by Lemaitre *et al*. (2007).

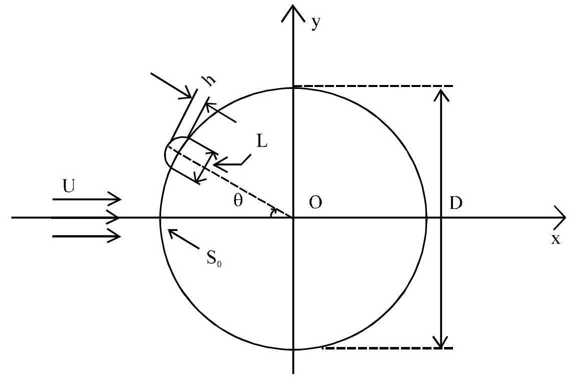

Fig. 1: Physical model of cable-rivulet system

Governing equations: The value 6.8×10^4 of Reynolds number based on cylinder diameter D and incident velocity U is selected which indicates that the flow is subcritical, therefore turbulent modeling must be considered. Thus Large-Eddy Simulation (LES) method is employed for the flow simulation. The filtered incompressible N-S equations in dimensionless form are:

$$\begin{cases} \dfrac{\partial \bar{u}_i}{\partial x_i} = 0 \\ \dfrac{\partial \bar{u}_i}{\partial t} + \dfrac{\partial \bar{u}_i \bar{u}_j}{\partial x_j} = -\dfrac{1}{\rho}\dfrac{\partial \bar{p}}{\partial x_i} + \dfrac{1}{Re_D}\dfrac{\partial^2 \bar{u}_i}{\partial x_j \partial x_j} - \dfrac{\partial \tau_{ij}}{\partial x_j} \end{cases} \quad (i=1,2,3) \qquad (1)$$

where, $\bar{u}_i$ are the filtered dimensionless velocity components in Cartesian coordinates along the i-th direction (i = 1, 2, 3 corresponding to x, y, z direction), $\bar{p}$ is the filtered pressure, ρ and ν are the density and kinematic viscosity of the fluid, respectively, τ_{ij} is the SGS stress.

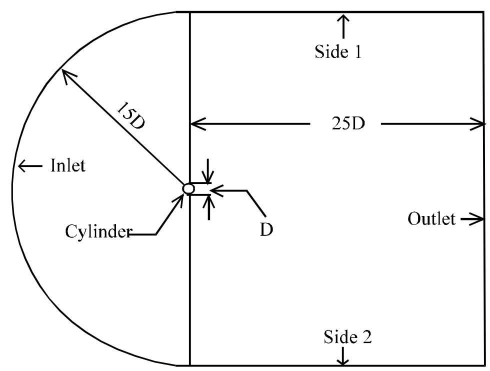

Fig. 2: Computational domain in axial view

Computational domain and discretization: The computational domain is shown in Fig. 2. For the purpose of producing smooth and structural grid, a semi-cylinder computational zone with radius of 15D is selected in the upstream of the cylinder and a rectangular computational zone is used in the downstream of the cylinder where the outlet of the zone is set at a distance of 25D away from the cylinder center. The scale of the computational zone in the axial (span-wise) direction is set as 5D. The first layer of the grid in the normal direction to the cylinder surface is located at a distance $y^+\approx1$ from the cylinder, where, y^+ is a dimensionless length based on wall shear stress and flow viscosity.

Finite volume method is introduced for spatial discretion and the SIMPLEC algorithm is applied to uncouple the pressure-velocity equations. A second order upwind scheme is used for both velocity and pressure spatial discretizations and a second order implicit scheme is employed for the temporal part. Dirichlet boundary condition is taken at the inlet boundary, i.e., u = 1 and v = w = 0 and Neumann boundary conditions are applied at other boundaries where the normal gradients of all variables are assumed to be zero. No-slip boundary condition u = v = w = 0 is used at the cylinder surface.

Items:

- Reynolds number (Re):

$$Re = UD/\nu \tag{2}$$

- Strouhal number (St):

$$St = fD/U \tag{3}$$

where, f is primary frequency that lift force vibrates.

Force coefficients: Assuming that F is the drag or lift force on the cylinder, then the force coefficient will be:

$$C = \frac{F}{\frac{1}{2}\rho U^2 A} \tag{4}$$

where, A is the frontal area. In present study C_D and C_L are used to represent drag and lift force coefficients. Similarly, the surface friction coefficients C_F is defined using surface friction E_f. The fluctuations of lift and drag force coefficients which are given by the root mean square values are identified with C_{DF} and C_{LF}.

Pressure coefficient (C_p): Let p_∞ be the far away pressure of incident flow and p be the total pressure, then the pressure coefficient is given by:

$$C_p = 2\,(p-p_\infty)/(\rho U^2) \tag{5}$$

VALIDATION

Validation is carried out first with a plain circular cylinder. This part focuses on both the efficiency of numerical methods and the grid resolution independency. Four different grid systems are examined named Test-A, B, C and D listed in Table 1. Test-A, B and C have the same circumferential grid but different axial grids. Test-D has medium axial grids and less circumferential grids.

The resulted force coefficients and Strouhal number are presented in Table 2, where some results from literature are also presented for comparison. It is seen that the value of C_D with fine axial resolution (Test-C) is close to the experimental results with similar Reynolds number, i.e., only 1.6 and 4.9% lower than that of Lam *et al.* (2003) and Alam *et al.* (2010), respectively. The value of C_D with moderate axial resolution (Test-B) is also close to the experimental data, i.e., 5.8% lower than that of Alam *et al.* (2010). A much higher C_D value may be obtained when the axial resolution is coarse which suggests that such low axial resolution should be avoided. A slight lower circumferential resolution (Test-D) is tested and the C_D is very close to that of Lam *et al.* (2003). This slight reduction of circumferential grid resolution will help reducing computational cost. The comparison of C_{Lf} for different tests with the experimental data indicates similar trend. Basing on the vortex shedding frequency which is given by applying FFT onto time varying lift force coefficients, the values of St from the tests show well agreement with those from the literature. Considering both the calculation expense and accuracy, a mesh system with fine grid in XY plain and moderate grid in Z direction are adopted for further simulation.

Table 1: Details of different grid system tested

	Grids			
Cases	Axial	Circumferential	Planar	Total
Test-A	40	200	20080	803200
Test-B	60	200	20080	1204800
Test-C	80	200	20080	1606400
Test-D	60	160	17760	1065600

Table 2: Comparison of present results with existing experimental data

Cases	Re_D	C_D	C_{Lf}	St
Lam *et al.* (2003)	4.1×10^4	1.19	0.38	0.20
Alam *et al.* (2010)	4×10^4	1.15	0.2	0.199
	6×10^4	---	0.3	0.209
Test-A		1.2626	0.4205	0.2200
Test-B	6.8×10^4	1.0657	0.3518	0.2118
Test-C		1.1315	0.3754	0.2231
Test-D		1.1923	0.3595	0.2044

RESULTS AND DISCUSSION

Aiming to both investigate the effect of orientation angle of the rivulet attachment on the flow pattern around cylinder, four different attached angles where, θ = 0, 30, 45 and 60° are examined. The forces on the cylinder and flow field around the cylinder are analyzed.

Forces and strouhal numbers: Mean drag force coefficients, C_D, fluctuations of drag and lift forces, C_{Df} and C_{Lf}, are shown in Fig. 3. It is seen that, the trend of C_D varying with θ is quite similar to the results of Alam *et al.* (2010). It is also found that rivulet makes C_D much lower than that of plain cylinder when attached angle θ is below 45°. When, θ = 45° C_D is slight higher than that of θ = 30°. At θ = 60°, C_D bounces to 1.616 which surpasses that in plain cylinder situation and this value is more than twice that of smallest one at θ = 30°. C_{Df} of rivulet attached cases are close to that of plain cylinder except when the attached angle is 60°. When θ = 60° C_{df} goes to many

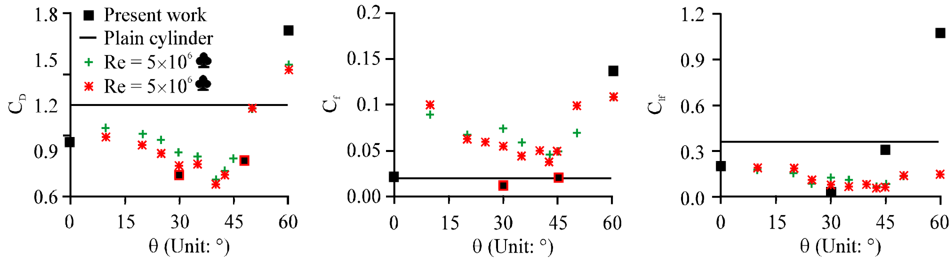

Fig. 3: C_D, C_{Df} and C_{Lf} varying with θ. (♣: Alam *et al.* (2010)

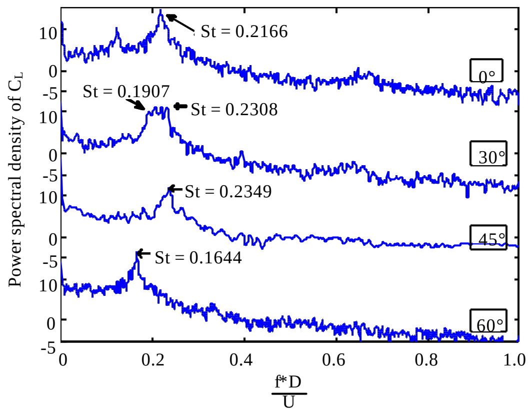

Fig. 4: Spectrum of lift force coefficients

times higher than that of plain cylinder. C_{Lf} also shows a sudden change at θ = 60° and its value is about twice larger than that of plain cylinder.

The frequency spectrums of lift force via FFT calculation are shown in Fig. 4 and the primary peak frequency corresponds to the Strouhal Number. When θ = 0° St is close to that of plain cylinder. While the attached angle is equal to 30°, there is no peak frequency where the spectrum density is of priotity, instead in a frequency band from 0.1907 to 0.2308 the density keeps at a similarly high level. The largest *St* of steady case appears at θ = 45° with the value of 0.2349, then St suddenly drops 30% to 0.1644 at a higher attached angle of 60°. This trend is quite similar to the experimental results of Alam *et al.* (2010), where two tripping rods were symmetrically placed at the cylinder face mainly to analyze how the rods position affected the flow field and forces onto the cylinder at various Reynolds number.

Pressure and surface friction: Basically aerodynamic forces acting on cylinder can be distinct in two parts the pressure and the friction. Their distributions on the cylinder face will help revealing forces vibrations among cases. For the convenience of description the 3D cylindrical surface in Cartesian coordinate is converted into 2D rectangle with circumferential direction (Φ) and axial direction (Z which is normalized with cylinder length). The circumferential coordinate origin form the front stagnation point S_0 (Fig. 1) of Φ = 0 with the clockwise direction and end at the same point of Φ = 2π.

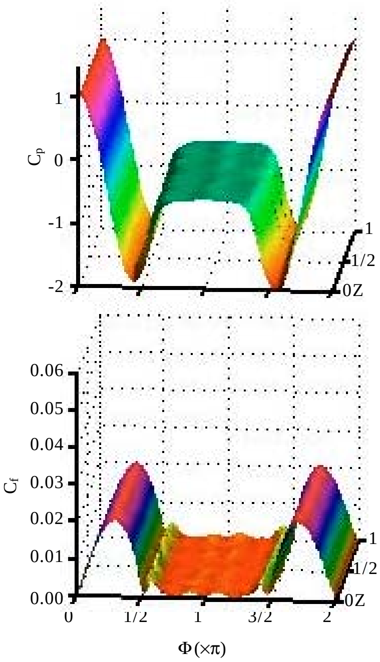

Fig. 5: Pressure and friction coefficients on surface of plain cylinder

For plain cylinder, it can be seen from Fig. 5 that both C_p and C_f distribute symmetrically about the back stagnation line (Φ = π). When there is a rivulet attachment, C_p suddenly drops at the rivulet position (Fig. 6a). At θ = 0°, C_p distribution is almost symmetricand its symmetry is wrecked as θ grows up. When θ = 30°, pressure quickly recovers a little then withdraws to minimal value at Φ = π/2, after that recovers again and keeps average at trailing zone of the cylinder. While θ = 45°, C_p comes up to average level directly behind the rivulet. And C_p distribution looks quite different at θ = 60°comparing other cases with lower θ, not only C_p

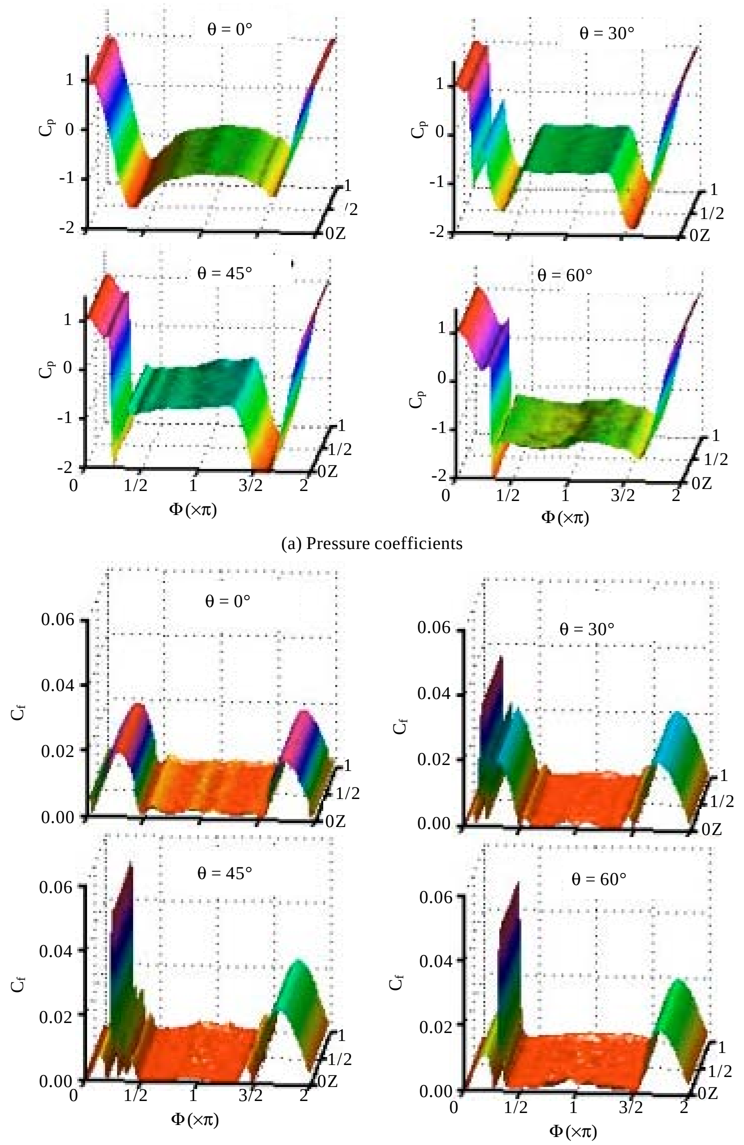

(a) Pressure coefficients

(b) Surface friction coefficient

Fig. 6(a-b): Pressures and friction coefficient distributions at cylinder surface with rivulets

distribution at trailing edge zone is unbalanced which means the upper side ($\pi/2<\Phi<\pi$) is slight lower than the down par t($\pi<\Phi<3\pi/2$) but also its value is smaller than previous cases. This directly leads to the sudden increase of C_D. For the frictional coefficients (Fig. 6b), letting aside for the rivulet neighborhoods, C_f distributions at back-and-down part ($\pi/2<\Phi<2\pi$) vary not much via cases. When the rivulet is at the most forward, both steady and oscillating cases have almost the same configuration as plain cylinder.

Wake dynamics: Wake dynamics is very important in bluff flow investigation and it will help revealing not only the forces and vibrating properties of cylinder but also reaction of cylinder to fluid field. Wake dynamics of plain circular cylinder have been studied a lot and different regimes are classified as *Re* varies. As Williamson (1996) reviewed: after laminar and wake transition regimes, the flow underwent shear-layer transition regime in a long range of Re (1,000---200,000) where in present work it locates; then as Re continuously grew, boundary layer

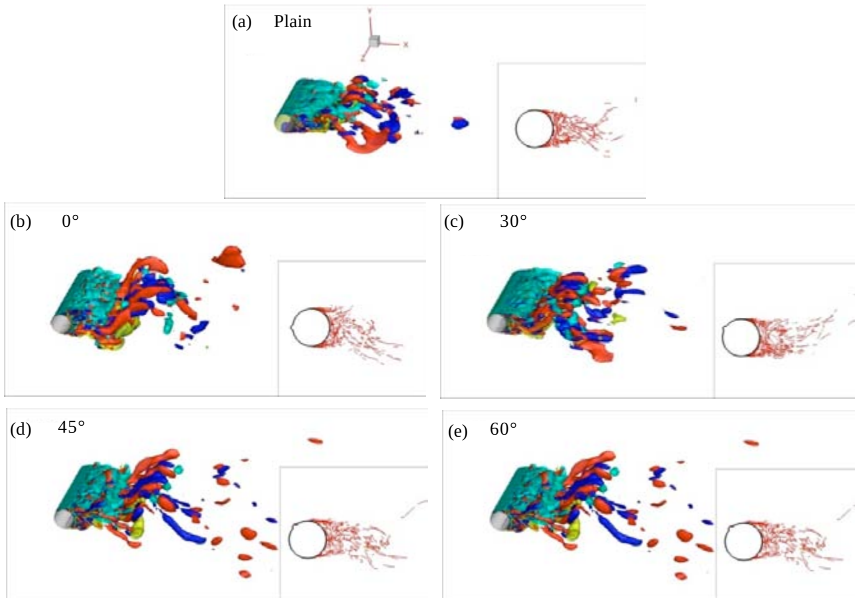

Fig. 7(a-e): Iso-contour of instantaneous vortice, stream-wise: red (ω_x* = 2) and blue (ω_x* = -2); axial-wise: yellow (ω_z* = 2) and light blue (ω_z* = -2). Right down corners show the vortices cores from axial view

transition regime took place. However, when the rivulet is attached on plain cylinder, the boundary layer will be greatly changed, on concerning affection of rivulet to near wall region and the wake, both instantaneous and mean wake properties of the cylinder are investigated via different ways in this section, including pressure, velocity, vortex and vortex shedding frequency.

Instantaneous flow field: Iso-surface of vortex gives general information of flow formations, where vortex (ω) can be made dimensionless throught $\omega^* = \omega D/U$. Iso-contour of instantaneous vortex in stream-wise (ω_x*) and axial direction (ω_z*) are shown in Fig. 7. The axial vortex surfaces seem to be easier to break down in plain or low attach angle steady cases (Fig. 7a-d) and keep formational longer distance down to further field with larger attach angle (Fig. 7e) which means the later one have stronger vortices especially at the same side where the rivulet locates. The pattern of stream-wise vortices appears as hairpin in most cases. The "hairpin" are more stable when θ is low (Fig. 7a-c). Once θ exceeds 45° "hairpin" fractures easily which is probably because of larger disturbance caused by the rivulet attachment. Obviously the scales of the "hairin" which demonstrats the scales of near wake, are different varing with cases and an much easier way to get those information is from vortices core distributions (right-down corner in Fig. 7). Comparing with other cases when cylinder is plain and steady (Fig. 7a) the trans-flow length (L_T) of vortices core zone is narrow. Apparently vortices burst point along the cylinder face is put back compared with other cases. In Fig. 10b L_T is larger but the stream-wise length (L_S) of vortices core zone hardly changes. As θ increases (Fig. 7c,d) vortices congregate to the center line, L_T get smaller but still over that of plain cylinder. When θ reaches to 60° (Fig .7e), vortices suddenly diffuse around and L_T nearly doubles compared with previous case. Rather than that the vortices cores come out and reattach to the cylinder face behind rivulet attachment θ = 45° (Fig. 7d), when θ = 60° (Fig. 7e) the vortices zone behind rivulet radiate backward.

Mean flow properties: Forces and Strouhal number are closely connected with near wake parameters that include: formation length of mean recirculation region, recirculation bubble shape and wake width etc. The bubbles are recognized by the iso-surface of mean stream wise velocity ($U_{x,mean}$) with zero value. Three dimensional bubbles of different cases are shown in Fig. 8, where the right-down corner of each case gives stream wise slice through cylinder center line with negative $U_{x,mean}$ in blue color. It is seen that the bubble along the axial direction is uniform.

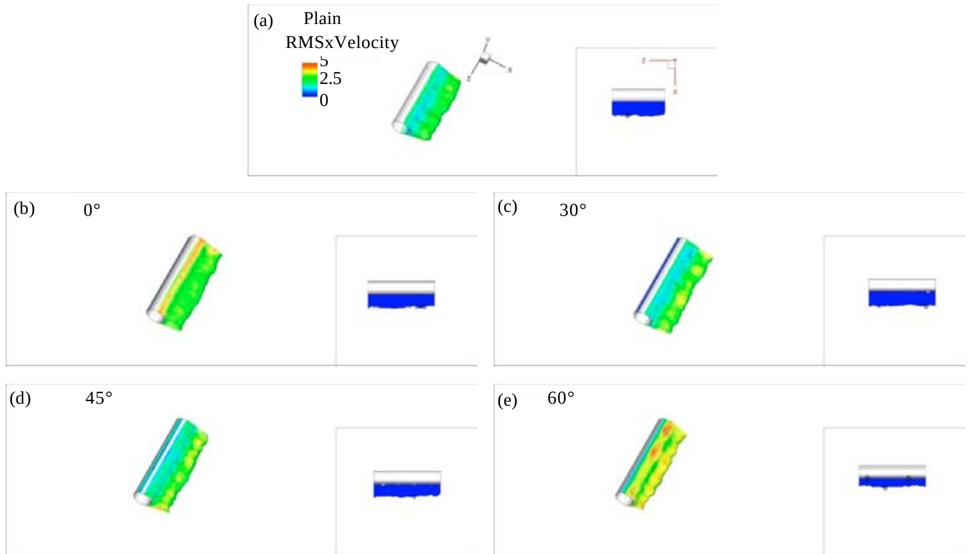

Fig. 8(a-e): Iso-surface of mean stream wise velocity $U_{x,\ mean} = 0$. Right down corner: stream wise slices through center lines of cylinders where blue zones show negative $U_{x,mean}$

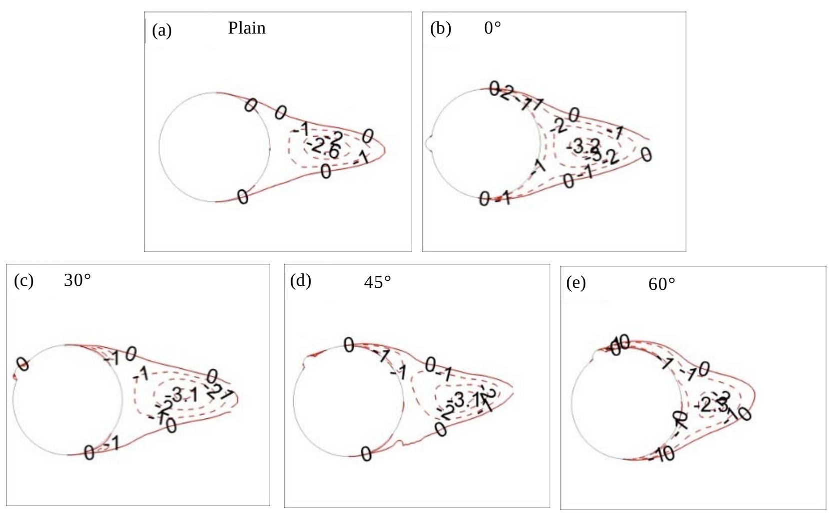

Fig. 9(a-e): Contours of $U_{x,\ mean}$ (non-positive) on axial cross section

The formation length (L_F) which expresses the stream wise scale of the recirculation region, can be defined as the distance from the most downstream point on zero value bubble face to the central line of cylinder. Zdravkovich (1997) pointed out that larger L_F corresponded smaller C_D, C_{Df} and C_{Lf} or vice versa. In this work L_F is gotten from the axial cross section of $U_{x,\ mean}$ contour shown as Fig. 9. For convenient description normalized value $L^*_F = L_F/D$ is used instead. L^*_F varies a little except decreasing suddenly at $\theta = 60°$ where C_D dramatically increases as recited previously and according to Table 3 it reduces nearly 30% at $\theta = 60°$ comparing with other attached angle. $U^*_{mean,\ min}$ which represents the minimum ratio of $U_{x,\ mean}$ to U, is also listed in Table 3 for comparison. It exposes that the largest value of $U^*_{mean,\ min}$ appears when $\theta = 60°$, at which it is nearly 40% larger than that of steady cylinder with smaller attached angle.

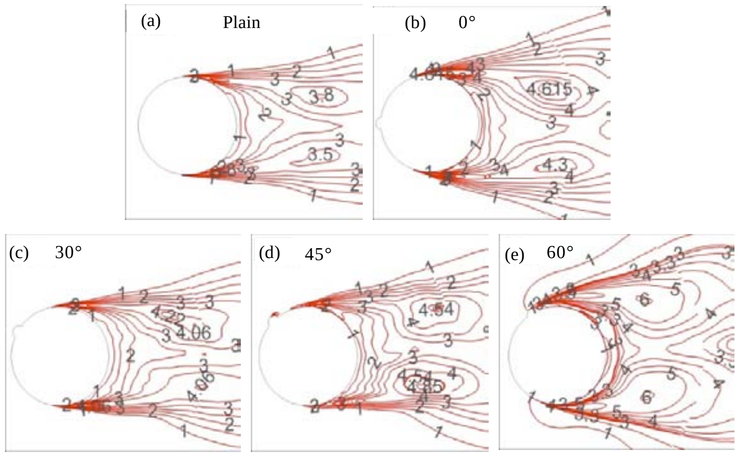

Fig. 10(a-e): Contours of $U_{x,\,RMS}$ on axial cross sections

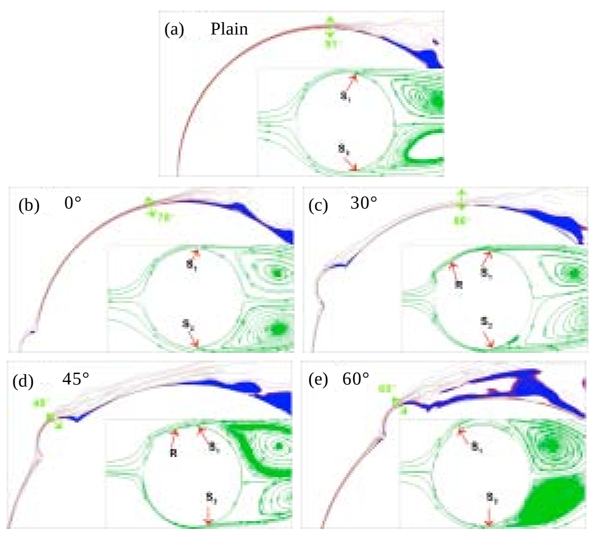

Fig. 11(a-e): Separation, reattaching and Boundary layer status: (S1, S2---up, down separation point; R---reattaching point; ↕---origin of laminar boundary transition)

Table 3: Details of wake parameters

	Plain	0°	30°	45°	60°
L^*_F	1.55	1.51	1.57	1.51	1.18
$U^*_{mean,\,min}$	-0.26	-0.32	-0.31	-0.31	-0.23
W^*_w	0.60	0.76	0.63	0.77	0.95
$U^*_{RMS,\,max}$	0.38	0.46	0.41	0.45	0.60
S1	102°	97°	99°	92°	60°
S2	257°	267°	258°	250°	261°
R	---	---	36°	70°	---

Width of the wake, W_w, is another important parameter and it can be defined in different ways. One way used by Alam *et al*. (2010) is to take the lateral separation between the two maximum concentrations of root mean square velocity in stream wise ($U_{x,\,RMS}$). $U_{x,\,RMS}$ contours on axial cross sections are shown in Fig. 10. The maximum $U_{x,\,RMS}$ and W_w are normalized using U and D and they are represented with $U^*_{RMS,\,max}$ and W^*_w of which the values are list in Table 3. Basically larger W^*_w corresponds bigger $U^*_{RMS,\,max}$ could be summed up. The max and the least appear at $\theta = 60°$ and plain case, respectively which W^*_w of the former is about 50% over than that of the later. Comparing the results here with those in Alam *et al.* (2010)'s experiment, good consilience of $U^*_{RMS,\,max}$ is received except at $\theta = 60°$, where in present study the value is much higher.

Boundary separation: Boundary separation and transitions in boundary layer is shown in Fig. 11, where S_1 and S_2 represent two separation points, R marks the reattaching locations, details of these angles that are defined with clock-wise direction front stagnation point are listed in Table 3. The down separation points, S_2, are not much varying, locating at near 260° in most cases. The upper separation points, S_1, are nearly the same when θ is 0° or cylinder is plain. At θ = 30° or 45° the boundary first separates at the rivulet position, then reattaches and separates again thereafter. The difference between those reattachments is in the former case a laminar flow reattaches on the cylinder face while in the later before the reattachment point the flow goes to transition already. This makes S_1 of the latter case appears several degrees ahead that of the former case. At θ = 60° the flow separates and goes to transition at the rivulet position which enlarges the wake behind the cylinder, therefore a large C_D comes out.

CONCLUSIONS

Numerical simulations about RWIV were carried out in this work using LES method. The effects of upper rivulet position, θ, to the flow pattern and to the forces acting on the cable are investigated. The results show that the existence of upper rivulet changes boundary separation and boundary layer transition. When the rivulet locate at the most front of the cable, the boundary layer is quite similar to that of the plain cylinder, thus similar flow pattern and aerodynamic forces are obtained. As θ goes little higher, the boundary layer separates at the position of the rivulet, then reattaches to the cable and the reattached boundary layer keeps laminar until it separates again. Similar situation of separation-reattaching-separation recurs as θ goes even larger, except that boundary turns to transition as past the rivulet before reattaching, thus the position that the flow separate again comes a little earlier. Then when θ is large enough, the boundary layer separates and makes transition directly after the rivulet. These properties of the boundary layer contribute to the different flow patterns and force properties of cable with various rivulet azimuths, where especially at θ = 60°, the force coefficients enlarges dramatically and Strohal number reduced a lot reasonably. Under the limitation of computational resource, only few rivulet attached angles are simulated. Further investigation with detailed attached angles should be conducted when larger computational resources are available.

ACKNOWLEDGMENTS

The study described in this study was supported by a grant from National Natural Science Foundation of China (Project number No. 90715031). The financial support is gratefully acknowledged.

REFERENCES

Alam, M. and Y. Zhou, 2007. Turbulent wake of an inclined cylinder with water running. J. Fluid Mech., 589: 261-303.

Alam, M., Y. Zhou, J.M. Zhao, O. Flamand and O. Boujard, 2010. Classification of the tripped cylinder wake and bi-stable phenomenon. Int. J. Heat Fluid Flow, 31: 545-560.

Alam, M.M. and Y. Zhou, 2006. Fluid dynamics around an inclined cylinder with running water rivulets. Proceedings of the ASME Fluids Engineering Division Summer Meeting, July 17-20, 2006, Miami, FL., USA., pp: 395-405.

Benazza, A., E. Blanco and M. Abidat, 2007. 2D detached-eddy simulation around elliptic airfoil at high reynolds number. J. Applied Sci., 7: 547-552.

Bosdogianni, A. and D. Olivari, 1996. Wind-and rain-induced oscillations of cables of stayed bridges. J. Wind Eng. Ind. Aerodyn., 64: 171-185.

Hikami, Y. and N. Shiraishi, 1988. Rain-wind induced vibrations of cables stayed bridges. J. Wind Eng. Ind. Aerodyn., 29: 409-418.

Islam, S.U. and C.Y. Zhou, 2009. Numerical simulation of flow around a row of circular cylinders using the lattice boltzmann method. Inform. Technol. J., 8: 513-520.

Lam, K., J.Y. Li and R.M.C. So, 2003. Force coefficients and Strouhal numbers of four cylinders in cross flow. J. Fluid. Struct., 18: 305-324.

Lemaitre, C., P. Hemon and E. de Langre, 2007. Thin water film around a cable subject to wind. J. Wind Eng. Ind. Aerodyn., 95: 1259-1271.

Li, H., W.L. Chen, F. Xu, F.C. Li and J.P. Ou, 2010. A numerical and experimental hybrid approach for the investigation of aerodynamic forces on stay cables suffering from rain-wind induced vibration. J. Fluid Struct., 26: 1195-1215.

Matsumoto, M., T. Saitoh, M. Kitazawa, H. Shirato and T. Nishizaki, 1995. Response characteristics of rain-wind induced vibration of stay-cables of cable-stayed bridges. J. Wind Eng. Ind. Aerodyn., 57: 323-333.

Matsumoto, M., T. Yagi, M. Goto and S. Sakai, 2003. Rain-wind-induced vibration of inclined cables at limited high reduced wind velocity region. J. Wind Eng. Ind. Aerod., 91: 1-12.

Robertson, A.C., I.J. Taylor, S.K. Wilson, B.R. Duffy and J.M. Sullivan, 2010. Numerical simulation of rivulet evolution on a horizontal cable subject to an external aerodynamic field. J. Fluid. Struct., 26: 50-73.

Shirani, E., 2001. Compressible flow around a circular cylinder. J. Applied Sci., 1: 472-476.

So, R.M.C., Y. Liu, S.T. Chan and K. Lam, 2001. Numerical studies of a freely vibrating cylinder in a cross-flow. J. Fluid Struct., 15: 845-866.

Williamson, C.H.K., 1996. Vortex dynamics in the cylinder wake. Ann. Rev. Fluid Mech., 28: 477-539.

Zdravkovich, M.M., 1997. Flow Around Circular Cylinders Volume 1: Fundamentals. Oxford University Press, Oxford, UK., ISBN-13: 978-0198563969, Pages: 694.

Zhan, S., Y.L. Xu, H.J. Zhou and K.M. Shum, 2008. Experimental study of wind-rain-induced cable vibration using a new model setup scheme. J. Wind Eng. Ind. Aerod., 96: 2438-2451.